

Dynamics of the Fe II 396.94 nm emission line observed at solar disk center

W. Schmidt and J. Fisher

Kiepenheuer-Institut für Sonnenphysik, Schöneckstr. 6, 79104 Freiburg, Germany
e-mail: wolfgang.schmidt@kis.uni-freiburg.de

Received 8 March 2013 / Accepted 23 September 2013

ABSTRACT

Aims. We have studied the structure and dynamics of the upper photosphere and lower chromosphere of the quiet Sun.

Methods. We analyzed a sequence of scans of slit spectra of the Ca II H line at 396.8 nm, with a spectral resolution of 850 000, and a spatial resolution of about one arcsec, taken in the quiet Sun at disk center, with a duration of about 55 min and an area coverage of $185'' \times 3.5''$. We used statistical methods to characterize size, lifetime, and dynamics of emission features of the Fe II line at 396.94 nm.

Results. We have identified about 780 distinct features where the Fe II line shows emission stronger than 3% above the local continuum. Their lifetime is on the order of one minute, and the spatial extent is about or less than $2''$. On average, Fe II emission features show a significant redshift of 1.3 km s^{-1} , with respect to the position of the absorption line. The redshift of the Fe II emission is absent close to the solar limb. The Fe II emission is coupled with a strongly enhanced intensity level of the Ca II wings. A time line analysis shows that other photospheric lines show significant redshift one minute before, and a blueshift after, the occurrence of an emission event. A redshift of the Ca II H line core precedes the redshift of the Fe II line by about 30 s. The occurrence of the H2v emissions is strongly reduced before and significantly increased after the Fe II emission events.

Conclusions. The temporal behavior of the Fe II emission line and both the Ca II H line core and H2v emission suggest a connection between Fe II emission and chromospheric activity. The presence of a significant redshift during the Fe II emissions and the absence of this redshift near the limb suggest that the observed redshift is indeed caused by a downflow in the line-forming region. From our result concerning the intensity fluctuations in the core of the Fe II line, and from the magnitude of the downflow velocities we conclude that the Fe II emissions at 396.94 nm occur in the photosphere.

Key words. Sun: photosphere – Sun: chromosphere

1. Introduction

In the chromosphere, the small-scale objects define the large-scale structure (Rutten 2012), i.e., a good understanding of the chromosphere as a whole requires detailed knowledge of the small-scale and short lived phenomena. This is a challenge both for observers and modelers.

With ground-based telescopes, the structure and the dynamics of the chromosphere and its well-known features (filaments, prominences, network, Ca bright points) are mainly observed in spectral lines like the hydrogen Balmer line at 656.3 nm, the He I triplet at 1083.0 nm, or the Ca II K and H lines at 393.3 nm and 396.8 nm. The photospheric spectral lines in the wings of the Ca II H and K lines, together with the calcium line cores, are known to provide height-dependent information about the solar atmosphere.

As pointed out in the review of Wedemeyer-Böhm et al. (2009), observations of the middle chromosphere that is dominated by shocks leading to the small-scale and short-lived phenomena mentioned above, require *high spatial, temporal, and spectral resolution all at the same time*. While this statement is certainly correct, the solar constant itself, i.e., the spectral flux density limits our ability to simultaneously meet these requirements.

Numerical 3D simulations of the chromosphere confirm the very dynamic behavior of the solar chromosphere. These simulations are almost always showing large fluctuations of temperature and density, caused by strong shock waves interacting

with cooler plasma (Wedemeyer-Böhm et al. 2009). On the other hand, semi-empirical models show smooth temperature profiles (Vernazza et al. 1981; Avrett & Loeser 2008).

Carlsson & Stein (1997) showed in their comparison of numerical simulations with observed spectra that Ca II H and H bright grains are generated by shock waves that propagate into downward flowing gas. At the location of the grains, the red emission peak (H2r) is very weak or absent. In their 1D model, the temperature drops with height, except during the grain-production episodes. As pointed out by Wedemeyer-Böhm et al. (2009), for example, the real situation is much more complex, since in 3D shock fronts are no longer plane-parallel.

Rezaei et al. (2008) presented long-slit spectrograms of the Ca II H line with high spatial and spectral resolution, where about a quarter of the line profiles taken in the interior of the chromospheric network do not have the central emission peaks that are the common signature of the chromospheric temperature rise. These reversal-free line profiles indicate that, at the locations where they were observed, the temperature rise was either shifted from the temperature minimum around 500 km upwards or did not exist at all. Thus the chromosphere apparently undergoes phases in which it is much cooler than in semi-empirical models, although probably not as cool as the coolest areas shown in some numerical simulations. In their Fig. 3, Rezaei et al. (2008) already presented a Ca II H line profile observed near disk center with a prominent Fe II emission, but did not discuss this further.

Besides long-slit spectrograms, narrowband filtergrams are often used to study the chromospheric dynamics. This technique provides large area coverage (compared to slit spectra) and high temporal resolution, but a certain mixing of photospheric and chromospheric contributions is unavoidable, as soon as the spectral bandwidth is larger than 0.5 \AA (Beck et al. 2013a). From a Ca II K filtergram sequence of an inter-network region with a width of 0.3 \AA , Wöger et al. (2006) describe bright grains with sizes of about $2''$ and a timescale of 53 s. The same time scale was found by Tritschler et al. (2007). This is about a factor of two longer the evolutionary time scale determined in the 3D model of Wedemeyer et al. (2004).

Using information derived from the spectral lines that are present in the wings in one of the Ca II lines provides strictly simultaneous and strictly co-spatial information about different layers of the solar atmosphere, since all lines are recorded on the same detector and all lines have similar wavelengths, such that the differential refraction caused by the Earth atmosphere is insignificant.

A special case of these lines is the weak Fe II line at 396.94 nm , located in the red wing of the Ca II H line. This line is mostly seen as an absorption line, but it turns into emission well within the limb. It was discovered by Evershed (1929). He observed the near-limb emission of this line. It was identified as a doublet Fe II line by Engvold & Halvorsen (1973). Stencel (1973) observed dozens of weak emission lines in the wings of Ca H and H near the solar limb, including the one at 396.94 nm . Rutten & Stencel (1980) catalogued several emission lines in the wings of the H and K lines. In their sample, the 396.94 nm showed the strongest emission. High-resolution observations of this line were made by Cram et al. (1980). They took a series of spectrograms of the Ca II H line across the solar disk. These authors were the first to report on the occasional emission of the Fe II line. They found a strong correlation of the spatial intensity variations with those measured in the wings of the Ca II H line, but no correlation with the intensity structure of the chromosphere seen in the Ca II H line core. From their observations and calculations, they concluded that the line is formed deep in the photosphere, in contrast to an earlier result of Lites (1974) who found a chromospheric origin of the Fe II 396.94 nm line on the basis of radiative transfer calculations. Watanabe & Steenbock (1986) found that the Fe II line is formed in the upper photosphere and therefore could be used as a diagnostics for that atmospheric layer; they also pointed to the relevance of this emission line as a diagnostic tool for the atmosphere of late-type stars. Stencel (1977) observed Fe II and other emission lines in the wings of the Ca II H and K lines of F, G, K, and M stars. From these observations he concluded that the Fe II emission lines provide information about the lower chromosphere. The 396.94 nm emission line has also been observed in solar flares (Švestka 1972).

In the past, the Fe II line at 396.94 nm has been observed or modeled as a static feature. In this paper, we present an investigation of the dynamic properties of emission events of that line observed at disk center. In Sect. 2.1 we describe the observations; our findings are listed in Sect. 3; and conclusions are drawn in the final section.

2. Observations and data reduction

2.1. Data properties

Observations were made at the German Vacuum Tower Telescope (VTT) in Tenerife in June 2007 and in November 2008. The Echelle spectrograph with a focal length of 7.5 m

Table 1. Data characteristics.

Parameter	Disk center data	Limb data
Date	2007-Jun.-14	2008-Nov.-09
Time	08:32–09:25	09:35–10:45
Spectral region	Ca II H, central part	
Position angle	1.0	0.0–0.35
Integration time	0.25 s	0.5 s
Slit width	0.5''	0.5''
Slit length	188''	188''
Scan step	0.5''	–
Scan width	3.5''	–
Image cadence	1 s	–
Scan repetition	8 s	–
Dispersion	0.4843 pm/pix	0.4843 pm/pix
Velocity scale	$365 \text{ ms}^{-1}/\text{pixel}$	$365 \text{ ms}^{-1}/\text{pixel}$
Spectral coverage	0.485	0.485 nm
Spatial coverage	$185'' \times 3.5''$	185''

was used to record spectra of the Ca II H line at 396.7 nm . A PCO4000 CCD (4008×2672 pixels, $36 \times 24 \text{ mm}$ chip size) was used in a 2×4 binning mode. The image scale at the spectrograph focal plane was $8.98''/\text{mm}$. This resulted in a spatial sampling of $0.332''$ per pixel. The slit width was $0.5''$ and the integration time was 0.25 s . Spectra were recorded using an order-selecting prefilter for the Ca II H line. The linear dispersion of the spectrograph is $D = 2f \tan \beta / \lambda$. With a focal length $f = 7500 \text{ mm}$, a grating angle $\beta = 63.4$ degrees, and $\lambda = 397 \text{ nm}$, we obtained a wavelength scale of 75.4 nm/nm in the focal plane, corresponding to a spectral pixel size of 0.484 pm . The spectral resolution of the data was determined by the pixel size to $\mathfrak{R} = \lambda / \Delta \lambda \approx 850\,000$. The adaptive optics system at the VTT (Berkefeld et al. 2003) provided good image quality and pointing stability. Scanning was done downstream of the adaptive optics system, and therefore did not affect the performance of that system. The angular resolution of the data was estimated from spatial power spectra to about $1''$.

Spatial alignment of the 400 maps along the spectrograph slit was not performed, since the pointing stability was very good most of the time. Image shifts perpendicular to the slit occurred twice during the time sequence. These shifts could not be corrected, but fortunately they do not influence our analysis which deals only with isolated and very short-lived phenomena.

Spectra for this work were recorded at disk center, in a region of very quiet Sun. The data include (a) large maps that cover an area of $185'' \times 120''$, and (b) sequences of short maps, with a cadence of 8 s and a width of 7 steps ($3.5''$). All maps were taken at a frame rate of one Hz, with the solar image moving across the slit in steps of $0.5''$. Additional limb observations of the same spectral regions, made in 2008, are presented here to illustrate the Fe II emission line, and for comparison with our disk center results. Table 1 summarizes the main parameters of our data. An example of a limb spectrum is shown in Fig. 1. The Fe II emission is nicely visible from the limb until about one arcminute toward disk center ($\cos \theta = 0.3$). This data is only used for a comparison concerning the position of the Fe II line in Sect. 3.4 below. The Fe II line at 396.940 nm belongs to multiplet 3 and has a lower excitation potential of 1.67 eV (Moore et al. 1966; Stencel 1973).

2.2. Data reduction

The present analysis concentrates on one of the short scans ($3.5''$ scan width), which was taken on 14 June 2007, between 8:32 h

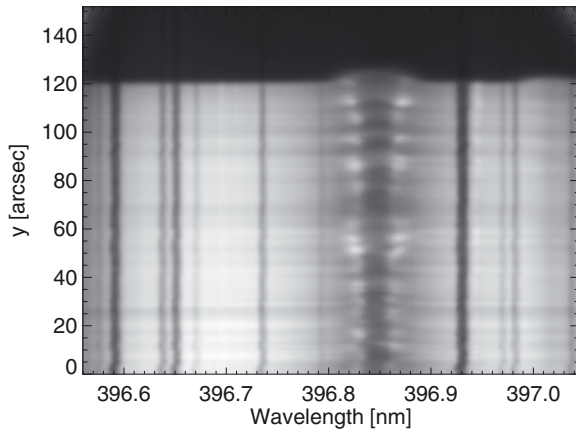


Fig. 1. Line core and inner wings of the Ca II H line recorded at the solar limb (northwest, latitude 60°). The Fe II emission is nicely seen at a wavelength of 396.94 nm. The off-limb emission of both the Ca H and the H ϵ lines are also visible.

and 9:25 h, with 400 repetitions and a duration of $400 \cdot 8 \text{ s} = 3200 \text{ s}$. The data were flat-field and dark corrected using standard techniques (Rammacher et al. 2007). The sequence contains two position changes, occurring after 28 and 40 min. These changes could not be compensated, since they contain motion perpendicular to the slit, which is irrecoverable. For the statistical analysis of the short-lived Fe II emission events these position changes are not relevant. After calibration, each spectrum covered a wavelength range from 396.6 nm to 397.7 nm and had a spatial coverage of 570 pixels, corresponding to $185''$. A slit spectrum is shown in Fig. 2, together with some line identifications.

2.3. Fe II emissions

In order to identify Fe II emission events, each of the 1 596 000 individual Ca II H line profiles was inspected, and we compared the line core intensity of the Fe II line with the intensity of the neighboring line-free pseudo-continuum, at a wavelength of 396.947 nm (control region). We introduced an emission strength factor, so that the strength of the emission could also be measured. If the mean intensity of the Fe II line was greater than 101.0% of that of the control region, it was named a 1% emission, and so on. Figure 3 shows the quantity of emission events found in the data sequence for various emission strength values. The histogram shows cumulative values, where all emissions having intensities greater than the specified emission strength are included, as well as discrete values, where the quantity is the number of emissions with exactly the indicated emission strength. Line profiles showing Fe II emissions stronger than 3% are plotted in Fig. 4 in a pseudo-2D diagram. The lower black line is the average line profile of the full data set. The upper line is the mean line profile for the emission events and shows a significantly enhanced intensity of the inner Ca II H line wings, weak H $2v$ emission, and virtually no H $2r$ emission. The Fe II line is seen as a faint absorption line at a wavelength of 396.94 nm. For comparison, a line profile from the Fourier-Transform-Spectrometer (FTS) atlas (Wallace et al. 1998) is shown as a red line. The line intensity is given in units of the continuum outside the Ca II H line. As our data does not include the continuum, the intensity was normalized to the FTS profile at a wavelength of 396.70 nm.

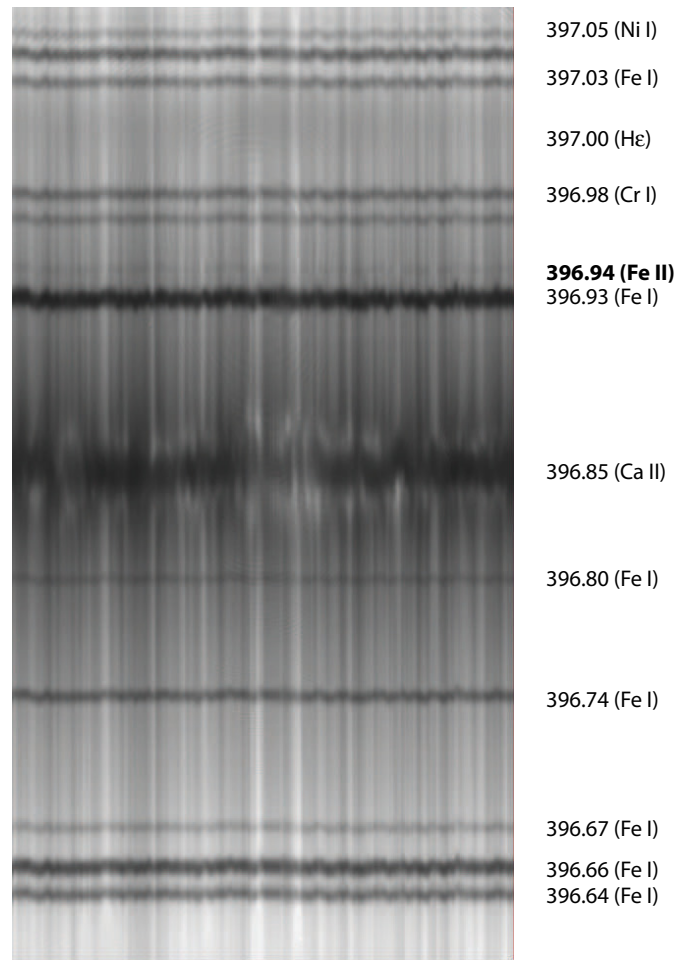


Fig. 2. Slit spectrum of the Ca II H line as used in this paper. The horizontal (spatial) axis covers about $180''$; the wavelength range is 0.47 nm. Some line identifications are indicated on the right.

3. Results

3.1. General properties of the time sequence

Before we proceed with the emission events, we briefly present some general properties of the data set. We show the temporal evolution of the slit spectra at several wavelength positions, and we compute the temporal power spectra for the same data. The Fe II emission events are included here. They are very rare and do not influence the general behavior of the solar atmosphere; they do so only locally and for a very short time, as will be shown below.

The top panels of Fig. 5 show the monochromatic temporal variation of the intensity measured along the spectrograph slit in the core of the Fe II line, and at a location in the blue wing of Ca II H, at a wavelength of 396.77 nm, at the same intensity level as the wing intensity near the Fe II line. The spatial intensity fluctuations measured along the spectrograph slit in the Fe II line core and in the blue wing of Ca II H at 396.77 nm are around 10% in both cases, in contrast to the findings of Cram et al. (1980). This means that both signals show the same temperature fluctuations and hence seem to originate in the same atmospheric layer, in agreement with Watanabe & Steenbock (1986) or an earlier finding by Lites (1974). The bottom panels of Fig. 5 show the temporal behavior of the H $2v$ emission peak and of the strong Fe I line at 396.93 nm. The former exhibits the familiar chromospheric pattern (a stable network region near $y = 105''$,

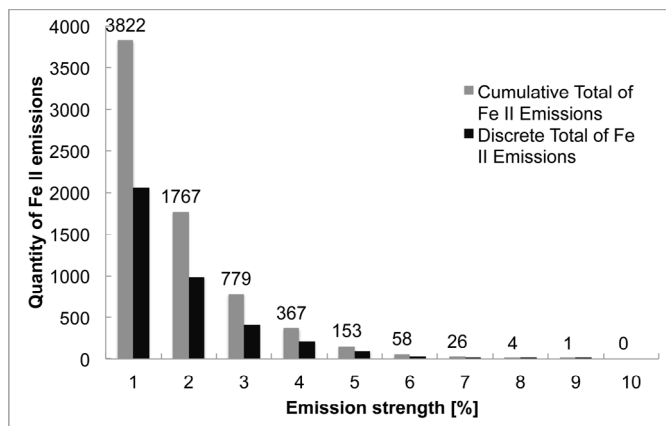


Fig. 3. Quantity of Fe II emission features identified in the data sequence. The horizontal axis denotes the emission strength (see text), and the vertical axis, as well as the labels above the bars indicate the number of events. The black bars are discrete and show the number of emission events with just the indicated strength; the grey bars are cumulative and show the number of events with emission strength equal to or greater than the value specified at each bar.

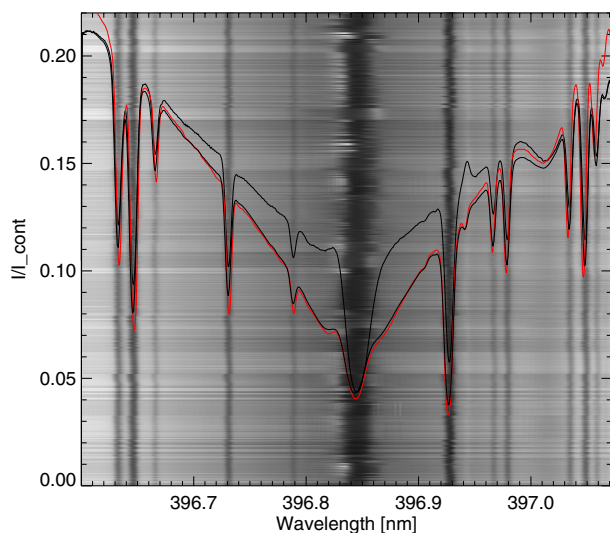


Fig. 4. Collage of several hundred line profiles showing an Fe II emission at 396.94 nm. The lower black line shows the mean line profile averaged along the slit and over the 3200 s sequence. The upper black line is the mean line profile of the emission events shown in this figure and shows a large increase in the inner Ca II H line wing intensity at the Fe II emission locations. An FTS atlas profile is shown as red line for comparison. We note the more or less complete absence of H 2r emissions at the emission events.

and short-lived bright grains in the inter-network), while the Fe I core still shows photospheric behavior with 5 min oscillations. The location of Fe II emission events for the slit position used for Fig. 5 is indicated by red contour lines. There are several examples, where the emission events re-occur at the same slit position, with a time difference around 200 s (e.g., $t = 16$, $y = 110$, $t = 40$, $y = 70$, $t = 50$, $y = 170$). Two examples of emission events are shown in Fig. 6. The bottom panels show the Fe II emission as a function of time, and the top panels contain the H 2v emission for the same time interval. The delay of the H 2v emission with respect to the Fe II emission is clearly seen.

Temporal power spectra of the intensity fluctuations are computed for the first 27 min of the sequence at each slit position

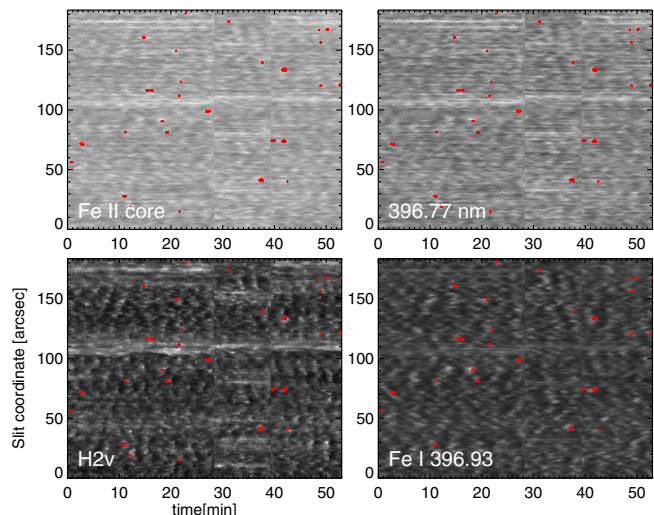


Fig. 5. Monochromatic space-time maps at fixed slit position for the Fe II line core, the blue wing of the Ca II H line, the Fe I line core at 396.93 nm, and the H 2v emission peak. The location of Fe II emission events is indicated by red contours.

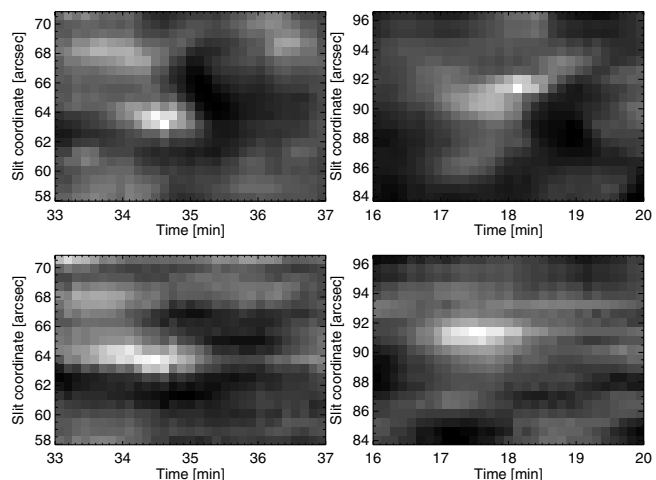


Fig. 6. Individual Fe II emission events (*bottom panels*), compared to H 2v emissions in the same time interval (*top panels*).

and for all spatial scan steps for the four wavelengths mentioned above, and also for the H ϵ line core. The power spectra are then averaged along the slit and across the scan positions for the five data sets (see Fig. 7). The behavior shown in Fig. 5 is confirmed: the power spectra of the Fe II line core (red line) and that of the blue wing position (grey line) are nearly identical with a maximum at 3.3 mHz corresponding to the 5 min oscillations, and significant power at low frequencies due to photospheric convection. The strongest 5 min signal is seen in the core of the strong Fe I line. The Ca II H core shows peaks at 3.3 and 6 mHz (5 and 3 min, respectively). For comparison, we also show the power spectrum of the core intensity of the H ϵ line with rather weak intensity fluctuations overall.

3.2. Characterization of emission events

The distribution seen in Fig. 3 shows that the number of emission events detected in the data sequence using these selection criteria decreases with increasing emission strength. The strongest emission event present in our data sequence has a total intensity across the Fe II feature that is between 9% and 10% greater than

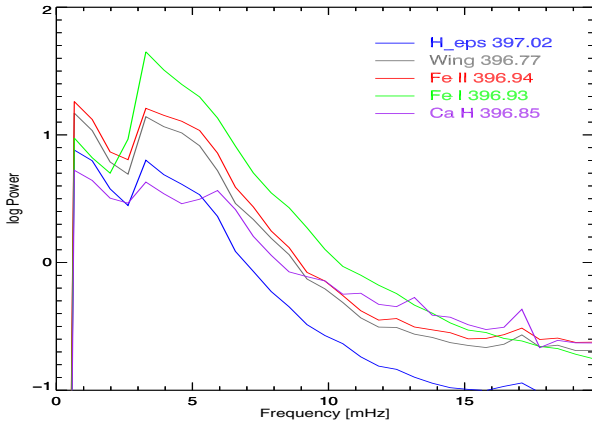


Fig. 7. Temporal power spectra of intensity fluctuations measured at the monochromatic wavelengths listed in Fig. 5, averaged along the spectrograph slit and the spatial scan coordinate. The power spectrum measured in the core of the He line is also shown.

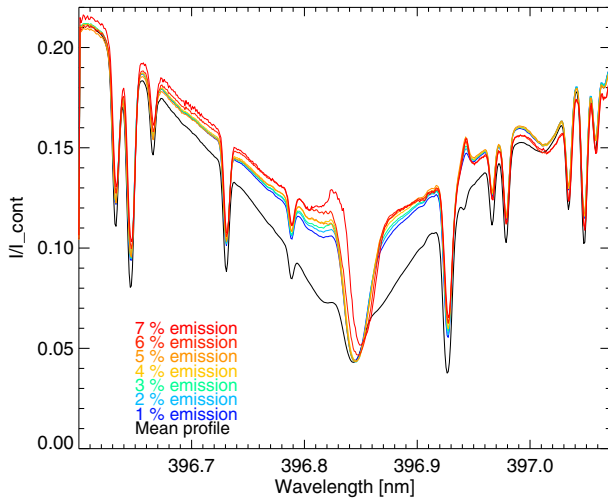


Fig. 8. Mean profiles of those that contain Fe II emissions for different emission strengths. The curves are cumulative, so that the 6% curve contains the 7% curve, etc. The average line profile for the data sequence is plotted for comparison. The intensity scale is normalized to the continuum, based on a comparison of our average line profile with an FTS atlas profile.

that of the control region. The line profiles belonging to the cumulative numbers were averaged to produce the mean profiles. A plot of the average profiles showing the Fe II line in emission at each of the different emission factors is shown in Fig. 8. The average Ca II H spectral profile across the entire data sequence is also shown for comparison. The profiles for the various emission strengths show little variability, and all of them are significantly different from the average line profile. As the emission factor increases, the line profile of the Ca II H wing background is shifted towards greater intensities, up to the 7% emission factor. The curves for 8 and 9% are omitted for clarity, but they are very similar to the 7% curve. The curves for the strong emissions show more noise, since there are only very few emission events with these strengths. An intensity increase of the line wing with increasing Fe II emission is obvious in the blue wing, but virtually absent at wavelengths above 397 nm. At this wavelength, the hydrogen line He of the Balmer series is formed, and this line (seen as a weak, broad dip at 397.01 nm) seems to get slightly stronger i.e., deeper with increasing emission factor. This effect

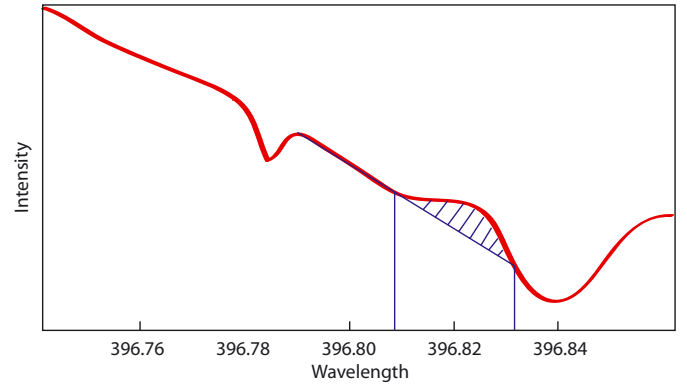


Fig. 9. Definition of emission strength of the H2v feature. The emission strength (hatched area) is the difference between the area between the vertical lines and the line profiles and the area between the line profile and the extrapolated line wing intensity.

may partly compensate the changes in the red wing intensity of the Ca II H line.

3.2.1. The 3% emission factor

In order to further study the properties and the effects of the emissions in the Fe II line, a large enough sample of them needs to be taken to ensure reliability of the results and statistics. The emissions themselves should also be strong enough so that they can reliably be called emissions. We identified 779 emission events in the data sequence using the 3% emission factor (Fig. 8), i.e., emissions with a strength of 3% or more were considered. This leads to a manageable, but large enough sample of events, and ensures that the emissions are strong enough to be studied in detail. From this point onwards, the term “Fe II emission profiles” always refers to this group of 3% emissions and the results and conclusions are based on findings from this sample. The locations of emission events in space and time are indicated in Figs. 5 and 10 for a fixed slit position.

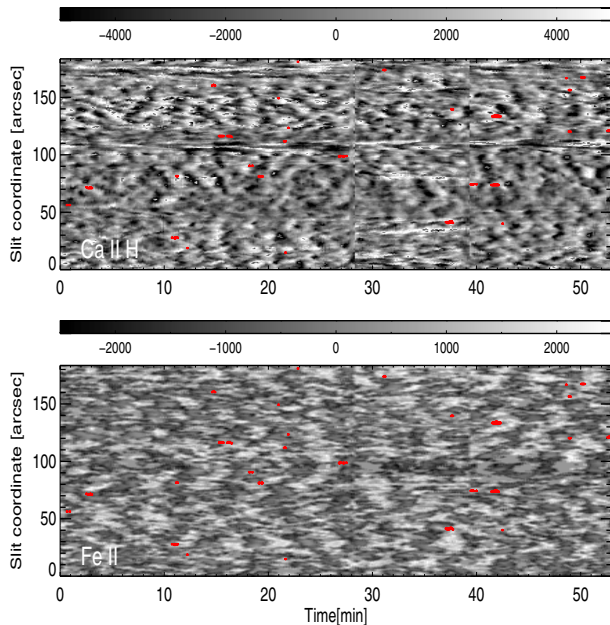
3.3. H2v emission strength

In order to determine the strength of the H2v emission, it is not sufficient to just measure the peak intensity, since this measurement does not make clear whether the emission itself is stronger, or if the whole line profile is shifted toward a higher intensity, or a combination of both. To measure the intensity of the H2v feature, we extrapolated the slope of the blue wing of the Ca II H line between 396.77 nm and 396.81 nm (the pseudo continuum) toward 396.83 nm, the average wavelength of H2v. The ratio between the peak intensity of H2v and the pseudo continuum at the same wavelength was then taken to characterize the emission strength. We also calculated the area between the profile of the H2v emission and the pseudo continuum as a more robust measure of emission strength (Fig. 9).

The measurements were made for (a) all 1 596 000 line profiles, (b) the 779 line profiles showing a 3% Fe II emission, and (c) a sample of 779 control locations. The results are summarized in Table 2. About 60% of all line profiles show an H2v emission, the same result obtained for the control locations, whereas only 36% of the lines with a 3% emission of the Fe II line are coupled with an H2v emission. However, where the H2v emission does occur together with an Fe II emission, it does so with greater strength than on average.

Table 2. Strength of H2v emission at those line profiles that contain an Fe II emission, compared to a control sample and to the entire data set.

Sample	Entire data sequence	Fe II emission locations	Control locations
Number of line profiles	1 596 000	779	766
Percentage of profiles with H2v emission	60.3	36.4	60.7
Mean ratio at H2v emission maximum	1.317	1.386	1.311
Mean ratio of areas under H2v line	1.25	1.27	1.22

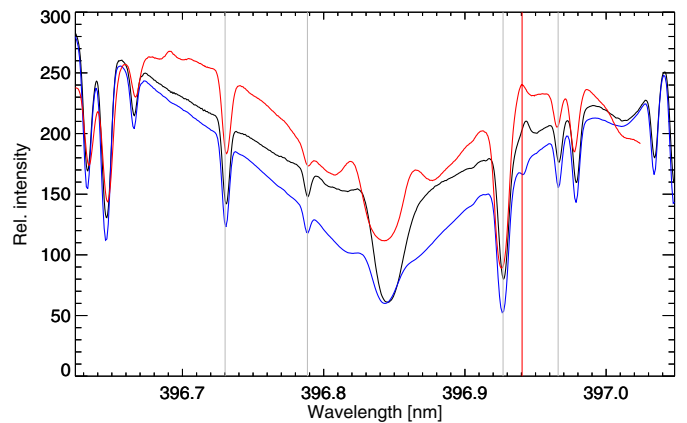
**Fig. 10.** Doppler velocity as a function of time for a fixed slit position. Fe II emission events are overplotted as red contour lines. *Top panel:* Ca II H line core velocity, *bottom panel:* Fe II velocity. The color bars above the panels indicate the velocity range in ms^{-1} .

3.4. Doppler shifts

In the analysis of line shifts we compared the Fe II line at 396.94 with the Ca II H line core positions, and with the positions of three neutral Fe lines, one in the red wing, and two in the blue wing of the Ca II H line. Line shifts were interpreted as Doppler shifts caused by line-of-sight motion of the gas in the line-forming region. The aim of this study was to find a possible connection between Fe II emission and material motion at the same location, but possibly at a different height in the atmosphere. All these lines are observed exactly at the same location in the $x - y$ plane, without a displacement by differential refraction in the Earth atmosphere, since they have very similar wavelengths.

The reference wavelengths for all Doppler shift measurements were obtained by averaging all line profiles of the sequence in space and time. The systematic effect of the varying line-of-sight component of Earth rotation is only on the order of 75 ms^{-1} and was neglected. The thermal drift of the spectrograph of the VTT is on the order of 50 ms^{-1} per hour (Doerr et al. 2012) and was also neglected.

The positions of the five lines were calculated by fitting a second order polynomial to the core of each line for all line profiles of all spectra in the data sequence. The polynomial fit was applied to a wavelength range of ± 7 pixels (6.78 pm) around the line core for the Fe lines and ± 15 pixels (14 pm) for the Ca line core. We then calculated the mean positions of the five lines for all spectra. A second mean value was derived for the 779 line profiles showing an Fe II emission (employing the 3% criterion).

**Fig. 11.** Comparison of the mean position of the Fe II line. The thick black curve is the mean of the line profiles with a 3% emission of the Fe II line; the lower curve is the average of all line profiles of our data set; and the upper curve is a spatial average of the same spectral region observed close to the solar limb. The grey vertical lines indicate the spectral lines used to align the wavelength scale of the limb profile. The vignetting of the limb profile is caused by the prefilter. The red vertical line shows the position of the Fe II absorption line at disk center, as well as that of the Fe II emission line at the limb. The redshift of the Fe II emission line at disk center is clearly visible.

The results are shown in Table 3, Cols. 1–4. The line shifts given in Cols. 4 and 7 are calculated as the difference between the mean (over the full data set) position of each line and the average position of the same lines when an Fe II emission was present. The Doppler velocity measured along the spectrograph slit as function of time is displayed in Fig. 10 for a fixed slit position.

A second method of calculating the mean positions of the lines under investigation was carried out in order to verify the results of the first method. Now we averaged all spectra of the sequence and then took the mean along the slit of the resulting averaged spectrum. The resulting line profile is shown in Figs. 4 and 11 as the lowest line. The mean of the 779 profiles showing Fe II emission was also taken and plotted in the same figure. The numerical results are shown in Table 3, Cols. 5–7. For the first method, the standard deviations are given for the mean line positions. These are not errors in the measurements, but rather the real scatter caused by Doppler motion in the solar atmosphere at different locations and at different times. Since the seeing was very good, and the spatial resolution was high, this scatter was to be expected. The precision of each individual Doppler measurement is about 0.08 pixels, corresponding to 30 ms^{-1} . The results of the second method mainly confirm those of the first one, but give higher redshifts for the Ca II H line core and for the Fe II emission line. This is not surprising, since the first method is subject to the noise in the individual line profiles. This noise is not negligible in both cases because of the low light level in the Ca II H line core, and owing to the weak signal of the Fe II line. In these cases, the second method is more robust, since it just averages a large number of profiles and only one least-square fit

Table 3. Shifts of the Ca II H line core and of selected spectral lines in the wings of the calcium line, measured at Fe II emission locations, compared to their mean positions.

Line	Mean pos. over all profiles	Mean pos. at Fe II emission location	Line shift [ms ⁻¹]	Line pos. in mean profile	Line pos. in averaged emission profile	Line shift [ms ⁻¹]
Fe I 396.68	135.97 ± 1.04	136.00 ± 1.14	11	135.94	135.95	3
Fe I 396.74	270.29 ± 1.15	270.42 ± 1.11	46	270.31	270.45	50
Ca II 396.85	502.75 ± 5.59	504.94 ± 4.86	797	503.11	506.48	1230
Fe I 396.93	675.01 ± 1.72	675.92 ± 1.92	333	675.08	675.97	325
Fe II 396.94	705.97 ± 3.37	708.71 ± 1.96	999	704.54	708.89	1590

Notes. In Cols. 2 to 4 and 5 to 7, respectively, different methods were used to derive the line positions. The methods are discussed in the text. Line shifts are given as Doppler velocities in ms⁻¹. The errors given in Cols. 2 and 3 are not the errors in the method; they show the scatter due to Doppler shifts in the solar atmosphere.

is performed. For these two lines, the second method is more reliable.

The comparison of the mean position for each of the lines with the position of the Fe II emission line is shown in Cols. 2 and 3 (or 6 and 7) of Table 3. The two Fe lines in the blue wing of the H line do not show any difference between total mean and mean of the emission profiles. The Ca II H line core is redshifted by about 1 km s⁻¹ during Fe II emission events relative to its average position. The Fe I line in the immediate vicinity of the Fe II line shows a small redshift of 0.9 pixels during emission events. The strongest effect is seen between the Fe II line in absorption and in emission, with a redshift on the order of 20 pm, corresponding to 1.5 km s⁻¹.

To double-check this surprising result concerning the redshift of the Fe II emission profile compared to the mean position of that line, we analyzed a completely different and independent data set of the same spectral region, but observed at the solar limb (Fig. 1). The Fe II emission is quite prominent, and so are the H2v and H2r emissions. The limb spectrum was recorded at a latitude of about 60 degrees north, but the exact location is not known. To eliminate the unknown influence of solar rotation on the observed wavelengths, we aligned the disk-center and the limb spectra in spectral dimension using several photospheric lines in both wings of the Ca II H line with a precision of about one third of a pixel (≈ 100 ms⁻¹). A comparison of the spatially averaged limb profile with the mean profile of the whole disk-center sequence and the average profile of the 799 emission events is shown in Fig. 11. This alignment also eliminates the influence of the limb effect on the Fe lines, except for a possible differential limb effect between the Fe I lines and the Fe II line, which is on the order of 150 ms⁻¹ (Balthasar 1984). Using the same analysis as before, we find the Fe II emission line near the limb very close to its nominal position. The red vertical line marks the position of the Fe II line in the mean disk center spectrum and in the limb spectrum. The redshift of the Fe II emission at disk center is clearly visible. This finding supports the idea that the Fe II emission at disk center is indeed caused by a downflow that is seen as a Doppler shift at disk center, but not at the limb, where the line of sight is perpendicular to the downward motion.

A closer inspection of our limb data also showed that the Fe II line is always in emission only for limb distances below 15'' ($\mu \leq 0.18$) (see Fig. 12), whereas Stencel (1973) reported the line to be in emission for $\mu \leq 0.4$, using data with much less spatial resolution.

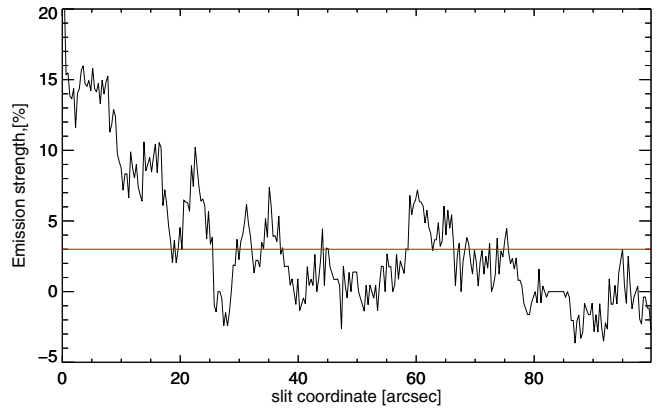


Fig. 12. Emission strength of the Fe II line observed at the solar limb. The horizontal axis gives the distance from the limb, the vertical axis is the emission strength as defined in Sect. 2.1. Negative values correspond to absorption. The horizontal line indicates the 3% threshold used in this paper.

3.5. Temporal analysis

In the previous section we compared wavelength shifts or Doppler motions of several spectral lines observed at the same time. Since these lines form at different heights in the solar atmosphere, small-scale propagating perturbations that would affect both the Fe II line and, for example, the Ca line core, would not be observed at the same location at the same time. We therefore took advantage again of the temporal resolution of our data to perform a temporal analysis. In this section, the Fe II emission events were again treated as single events; no clustering in space or time was considered. The wavelength shifts of the previously analyzed spectral lines was investigated over some period of time before and after the Fe II emission events and, in addition, properties of the Ca H2v emission were studied.

3.5.1. Evolution of Fe II emissions

We investigated the average behavior the Fe II line at the 779 emission locations before and after the emission. We chose a period of ± 10 time steps on either side of the emission event, corresponding to ± 80 s. This interval was considered large enough to cover the whole development of the emissions and to cover any immediate effect associated with them. Starting from the emission events according to the 3% criterion, we traced the Fe II line backward and forward in time, and we identified the line to

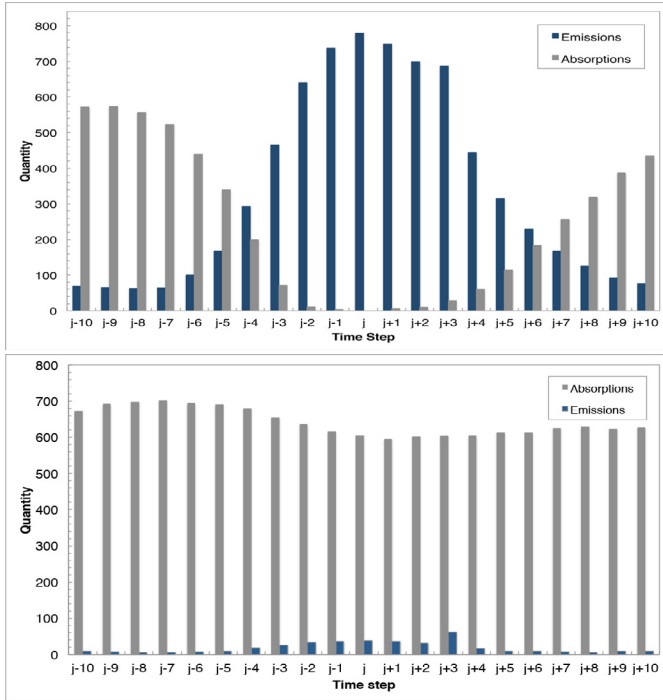


Fig. 13. *Top:* change of the Fe II line from emission to absorption (and vice versa) in an interval of ± 80 s before and after a 3% emission event of the Fe II line at time step j . The intensity thresholds for emission and absorption are 1.5% above or below the local continuum. The vertical axis denotes the number of emission or absorption features found at each time step. *Bottom:* the same relation, but for a set of arbitrarily chosen control locations.

be in emission, in absorption, or non-existent. The onset of an emission was defined to occur when the intensity of the line profile was higher than 101.5% of the neighboring continuum (cf. Sect. 2.1). Likewise, an emission ended when its intensity fell below the 101.5% threshold. An intensity of the line core below 98.5% of the continuum was taken as an absorption line, and values between these thresholds were considered as *no line*, since the spectral line was not easily identified in these cases. Figure 13 shows the result of this procedure, averaged over the emission events. The transition from absorption to emission is clearly seen and occurs on average at time step -4 , i.e., about half a minute before the 3% emission. The absorption line reappears at step $+7$, about one minute after the emission. The sum of the two bars belonging to the same time step does not always add up to 779; the differences are the *no feature* counts. Non-zero counts for both absorptions and emissions at the same time steps does not mean that we find both features at the same time. The counts show that in many cases the emission events are extremely short, about 30 s (four time steps), and long-duration events are rather rare.

To verify the reliability of our results, we applied the same procedure to a set of control locations. The lower panel of Fig. 13 shows that the number of identified absorptions is about constant, and the number of emissions is low. This is the expected result, as the control positions were chosen randomly in space and time. The histogram in Fig. 13 shows a gradual development and an average lifetime of the 3% emission events of slightly above 1 min.

3.5.2. Evolution of Fe II Doppler shifts

In a second step, we determined the temporal behavior of the line positions of both the absorption and emission features. As

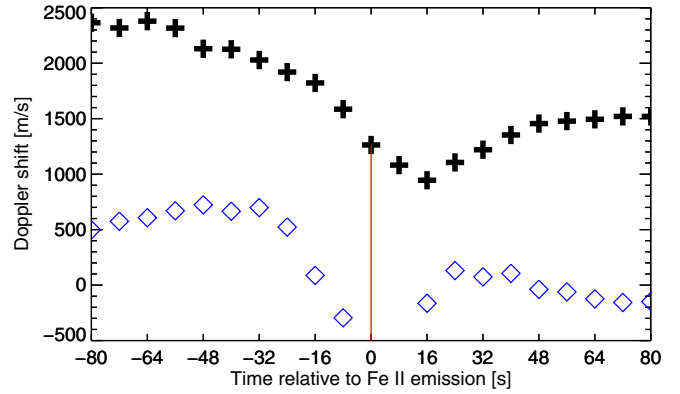


Fig. 14. Change of line position of emissions and absorptions, converted to Doppler shifts, of the Fe II line before and after a 3% emission at $t = 0$. The graph shows ten time steps (± 80 s) before and after the emission event (indicated by a vertical red line). The mean positions for all 799 emission events are displayed. The plus signs correspond to the emission profiles and the line positions of the absorptions are shown as blue diamonds. At $t = 0$ s and 8 s, there are no absorption profiles from which line positions could be derived.

in Sect. 3.4, the line position was calculated from a least-squares fit around the absorption minimum or the emission maximum. Figure 14 shows the line positions, averaged over all emission events, of the emission profiles as plus signs, and those of absorption profiles as blue diamonds. The line position is given in Doppler units relative to the mean line position given in Table 3, last line. Whenever the line is in emission, it is heavily redshifted already one minute before the 3% emission level is reached. The redshift decreases until about 15 s after the 3% emission level is reached and then levels off when the emission slowly fades away. Figure 14 has to be seen in context with Fig. 13: the very first and very last time steps of both figures contain only a few emissions. At $t = 0$ s, there are (by definition) no absorption profiles, and the time step at $t = 8$ s contains only a few absorption profiles; therefore, line positions for absorption are not shown in the figure. The absorption profiles at $t = -8$ s are slightly blueshifted, but only very few line profiles contribute to this measurement. Compared to the mean wavelength of the Fe II line measured in the full data set (shown as $v = 0$ in the figure), the emission features seen one minute before a 3% event are redshifted by about 2.3 km s^{-1} . The minimum redshift, at $t = 16$ s, is still about 1.25 km s^{-1} . There are virtually no emission profiles before $t = 80$ s, but it is obvious that the emission line is always heavily redshifted compared to the absorption profiles that are seen immediately before or after an emission event. This cannot be caused by a systematic error introduced by the measurement procedure, combined with the influence of the neighboring Fe I line at 396.93 nm. Such effects may exist, but they are well below one wavelength pixel (365 ms^{-1}).

3.5.3. The H2v emission before and after Fe II emissions

We also analyzed the intensity of the H2v emission at \pm ten time steps, or 80 s, around a 3% Fe II emission, and compared the results to a set of control locations. We used the method described in Sect. 3.3 for the calculation of the emission strength, where we showed that locations with an Fe II emission showed fewer H2v emissions compared to the average occurrence of H2v. The blue bars in the histogram in Fig. 15 show the percentage of Fe II emissions that are coupled with an H2v emission. Time step 0 (red bar) corresponds to the occurrence of a 3%

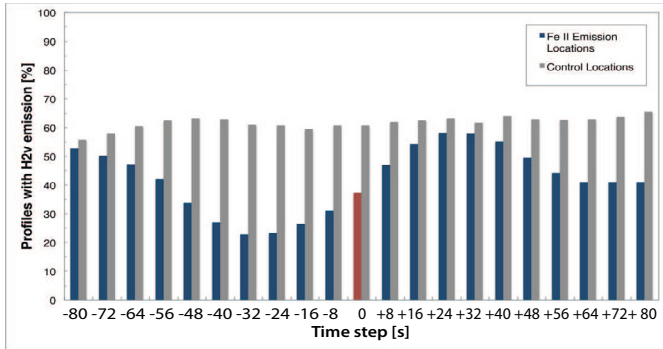


Fig. 15. Temporal relation between Fe II emission events and Ca H 2v emissions. The Fe II emission occurs at time step 0. There is a clear decrease of Ca H 2v emissions before and a significant increase after a Fe II emission event. The graph shows the average behavior of all 779 Fe II emissions. The grey bars show for comparison the time line of H 2v emissions of an equal-sized control group that is not co-spatial with Fe II emissions.

Fe II emission. The percentage of Fe II emissions coupled with an H 2v emission show a distinct oscillatory pattern. Preceding the Fe II emission, the H 2v emission reaches a minimum of about 23% 30 s before the 3% emission. After these emissions, the percentage of locations coupled with an H 2v emission increases and reaches a maximum of about 60% after 30 s. Thereafter the percentage decreases again. This pattern shows that before and during an Fe II emission, the chromosphere that is responsible for the occurrence of the H 2v emissions is much quieter or inactive than on average. The interval of about 60 s between minimum and maximum corresponds to the lifetime of the Fe II emission shown in Fig. 13. To verify the validity of this result, we repeated the same procedure at a set of control locations. The grey bars in Fig. 15 show no temporal variation and the numerical value of about 60% agrees well with the numbers given in Table 2.

We already noted in Sect. 3.2 that Fe II emissions often reappear at the same location at a later time. The oscillatory pattern of the ratio between Fe II and H 2v emission may in part be caused by this repetitive behavior.

We analyzed the temporal behavior of the strength of the H 2v emissions in the same manner as the occurrence, with a very similar result: the H 2v emission strength assumes a minimum about four time steps (32 s) before a 3% emission, and reaches a maximum four time steps after an Fe II emission.

3.5.4. Comparison with other lines

Finally, we compare the line shifts of the Fe II line with those of its neighboring Fe I line and with the Ca II H line core. We did not include the H 2v feature in this comparison. Its position is often very poorly defined, because the emission is quite weak. The wavelength shifts of the Ca II H line core and the Fe I line at 396.93 nm are measured at the locations of Fe II emissions before and after these emissions. Figure 16 shows spectral time slices for three individual Fe II emission events. The left panels show the Ca II H line core region, and the right panels show the corresponding Fe II line together with the neighboring Fe I line. The two lower rows correspond to the emission events displayed in Fig. 6; the top row is an additional example with a very strong emission (7%) and virtually no H 2v emission. The H 2v emission lags behind, as discussed in Sect. 3.5.3 above. The enhanced intensity of the line wings close to the Ca II H core resembles closely the well-known mustache phenomenon seen in H α or

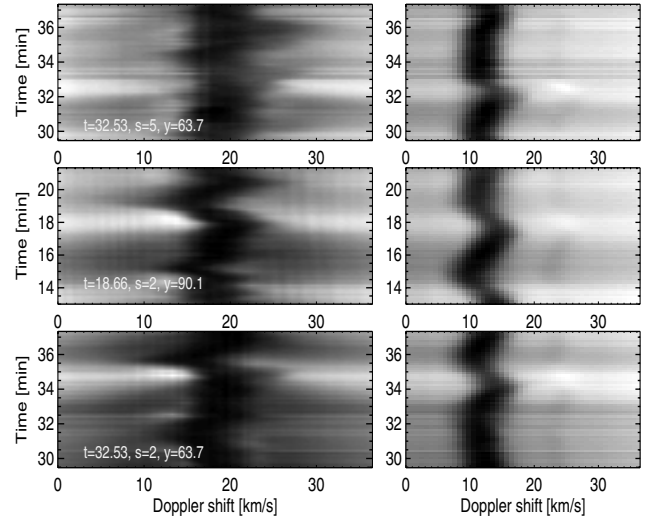


Fig. 16. Spectral time slices of three individual emission events. *Left panels:* Ca II H line core; *right panels:* Fe I 396.93 nm line and Fe II line. The horizontal axis is scaled in Doppler velocity. The inserted text provides the time of the maximum Fe II emission, (in min, counted from the beginning of the sequence), the corresponding scan step, and the slit position (in arcsec). The two *bottom rows* show the same emission events as Fig. 6.

H β (Severny 1956; Kneer 2010). Mustaches are observed in active regions or network boundaries, whereas our observations are made in inter-network regions of very quiet Sun. Mustaches observed in H β are linked to strong chromospheric downflows (Schmidt et al. 2000), whereas the mustache-like weakening of the Ca II H line in our data is associated with a photospheric downflow. Beyond these similarities, there does not seem to be any relation between the two phenomena. Except for the visual impression, there does not seem to be a relation between mustaches and the weakening of the Ca II H line in connection with Fe II emissions.

The mean line positions of these lines for all emission events over an interval of ± 10 time steps (± 80 s) are shown in Fig. 17. The vertical red bar marks the time step at which the Fe II emission occurred. Line positions are converted to Doppler shifts, relative to the mean positions of both lines of the full data set. On average, the Ca core (black plusses) is slightly blueshifted 80 s before the Fe II emission events, redshifted by about 0.5 km s^{-1} at the maximum of the Fe II emission, and considerably blueshifted by more than 1.5 km s^{-1} one minute after the emission. The behavior of the Fe I line (blue diamonds) is quite different and seems to be phase shifted relative to the Ca line core. About 30 s before the emission maximum, the line is redshifted by about 1 km s^{-1} . A maximum blueshift is reached 50 s after the emission. The figure also shows a set of control locations of the Ca line core (small plusses) and of the Fe I line (small diamonds) that was analyzed to demonstrate the reliability of our results. The line positions at the control locations shows some temporal variation which is probably of solar origin, but their amplitudes are considerably smaller than the variability that occurs in context with the Fe II emissions. The Doppler shifts of the Fe II line and the neighboring Fe I line are more or less in phase (redshift followed by blueshift).

4. Discussion and conclusions

In this paper we present the first detailed analysis of emission events of the Fe II line at 396.94 nm as seen at disk center.

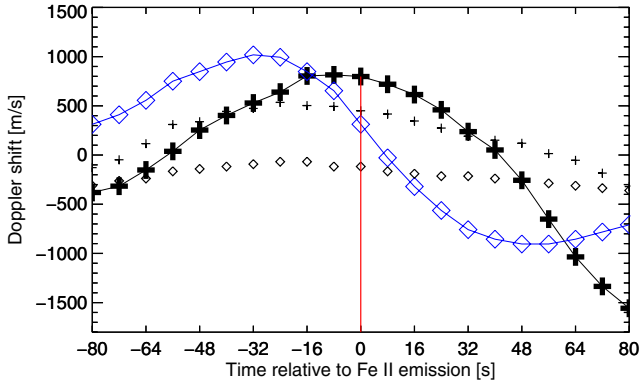


Fig. 17. Change of line position of the Ca II H line core (heavy black symbols) and the Fe I line at 396.93 nm (blue diamonds) before and after a 3% Fe II emission at $t = 0$. The graph shows ten time steps before and after the emission event (vertical red line). The small symbols show the line positions of a control group.

The aims included cataloguing the location and duration of the emissions appearing in this line, which is located in the wing of the strong Ca II H line core. Another aim of the investigation was to study the possible cause or effect of the Fe II emissions by observing the behavior of other spectral features within the Ca II H spectra. This was done with the view to identifying a link between the upper photospheric Fe II emissions and chromospheric dynamics. We used a statistical approach in order to establish an average description of the conditions in the solar atmosphere before, after, and during the Fe II emissions.

4.1. Measurement errors

The measurement error in computing individual line positions is about a tenth of a pixel. The error in the mean position shown in Fig. 14 is much larger, on the order of 1.5 pixels, due to the intrinsic variability of the observed wavelengths caused by solar oscillations and convective motions, for example. Since our observed emission events are distributed more or less randomly within the field of view and within the observed time interval, these processes do not introduce a systematic effect to our results. This is reflected in the smooth wavelength variation as a function of time shown in Fig. 14. The values for the line positions shown in this figure are in qualitative agreement with those presented in Table 3, but they are not identical, since the selection criteria used in this section are slightly different, as here we include weak emissions before and after the 3% events.

4.2. Comparison with chromospheric grains and supersonic events

In our data set which consists of a sequence of 400 maps with a size of $3.5'' \times 185''$ each, we find 779 events with emission stronger than 3%. These emission events are distributed more or less at random in space and time. Network areas do not show Fe II emissions. Our temporal analysis yields an upper limit for the lifetime of about 60 s (Fig. 13). Using this upper limit, we obtain an occurrence rate of 5×10^{-5} events per arcsec² per second. The spatial extent of the emission events is $2''$ or less. The intensity of the Fe II emissions is correlated to the Ca H line wing intensity, in agreement with Cram et al. (1980). As their findings were based on Fe II emissions seen toward the limb, and the conclusion from the present study is based on emissions seen at disk center, it can now be deduced for the first time that the correlation between the increased intensity of the Fe II emissions and

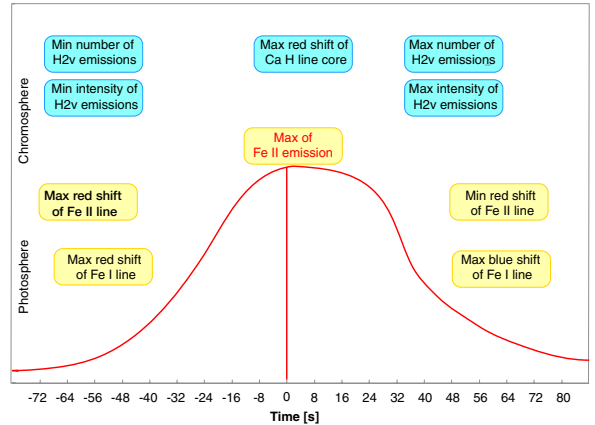


Fig. 18. Sketch of the temporal behavior of wavelength shifts and intensity changes of several lines in the wings of Ca II H before and after Fe II emissions. The red line is the envelope of the Fe II emission behavior depicted in the top panel of Fig. 13.

the increased intensity of the Ca II H wing background is valid across the whole solar disk.

The properties of the Fe II emissions outlined above stimulate a comparison of our findings with other episodic events in the solar atmosphere described in literature. On several occasions, the emission events reappear a few minutes later at about the same location on the solar surface. This behavior is reminiscent of the chromospheric Ca K grains in the interior of the chromospheric network described by von Uexkuell & Kneer (1995). They report on time differences between subsequent occurrences of 170 to 220 s on average, and three to five repetitions. Their findings concerning the occurrence of bright grains was confirmed by Beck et al. (2013b).

Figure 10 shows Fe II emission repetitions within 15 to 25 time steps, (corresponding to 120 to 200 s). Ca K (or H) grains are much more frequent than disk-center Fe emission events, so that only the temporal behavior is similar. On the other hand, Fe II emissions are very difficult to detect because they require observations of the Ca II H line at very good spatial resolution and high spectral resolution using a scanning slit spectrograph and such measurements are scarce. The number of Fe II emission events also depends strongly on the threshold (see Fig. 3) that is applied. That value, in turn, depends on the signal-to-noise ratio of the spectra.

Borrero et al. (2010) detected supersonic upflows which might be caused by magnetic reconnection in the photosphere in data obtained with the IMAx instrument of the Sunrise balloon telescope (Schmidt et al. 2010; Solanki et al. 2010). They find an occurrence rate of 1.25×10^{-5} for these supersonic upflows observed in the quiet Sun and a lifetime of 80 s. These numbers are not very different from our findings, but we do not want to speculate about a common cause, since our results given in Sect. 3.5.3 indicate a connection to the H2v emission and show a (subsonic) downflow associated with the emission events.

4.3. Temporal analysis

The main findings of our temporal analysis are summarized in Fig. 18, which describes how the dynamics in the atmosphere evolve before and after the Fe II emissions. There is downward motion in the photosphere before the Fe II emissions, and upward motion afterwards.

We assume that the variation of the H2v activity and the occurrence of a co-spatial Fe II emission have a common physical cause. Then the observed time lag of the peak strength of the

Fe II emission of either +30 s or –30 s to the maximum or minimum of the H2v activity indicates that the two events occur in different heights of the solar atmosphere. This is one more indication of a photospheric origin of the Fe II emissions. From the comparison of the intensity fluctuations of the Fe II line with those in the blue wing of the Ca II H line at the same intensity we also conclude that the Fe II line originates in the photosphere.

Figure 17 shows that the maximum redshift in the Ca II H line core occurs about 30 s before the maximum of the Fe II emissions. This result provides strong evidence of a direct link between the Fe II emissions and dynamic activity of the chromosphere. Additional dynamical effects in the chromosphere are seen through the variation in the H2v emission feature before and after the Fe II emissions (Fig. 15). Before the Fe II emissions, H2v emissions appear less frequently than on average, and with less intensity. The opposite situation occurs after the Fe II emissions. The overall conclusion that can be made is that the chromosphere is very quiet shortly before the Fe II emissions, becoming increasingly more active at times coinciding with the Fe II emissions, and reaching maximum activity about 30 s after the emissions. The notions *very quiet* and *maximum activity* have to be seen in context with the observed region of quiet Sun, with most of the emission events reported occurring in the inter-network, as can be seen in Fig. 10.

4.4. Final remarks

In the past, theoretical explanations of the Fe II emission line have concentrated on the static emission seen near the solar limb (see Sect. 1 for references). Based on this dynamical analysis of the short-lived Fe II events observed at disk center, a physical explanation for the short-lived emission events should now be found. Observations of the center-to-limb variation of this phenomenon (already suggested by Stencel 1973) would be most useful, but are difficult to obtain.

In the analysis of the Fe II emissions and absorptions, the emissions at disk center were found to be redshifted compared to the position of the absorption line. This redshift is on the order of 1.3 km s^{-1} . Rather than interpreting this phenomenon as the redshift being present due to the occurrence of an emission, it is more likely that the emission is caused by a downward gas motion in the line-forming region leading to the redshift of the line. Close to the solar limb, a downflow does not produce a Doppler shift, in agreement with the observed wavelength of the Fe II emission line there. Our high-resolution data obtained near the limb show that the Fe II line is constantly in emission only for $\mu \leq 0.18$ ($15''$ inside the limb, see Fig. 12), whereas Stencel (1973) finds the line in emission already at $\mu \leq 0.4$ ($80''$ inside the limb).

The existence of Fe II emissions points to an unusual state of the atmosphere: the source function above the line-forming region is increasing, for a short time and over a very small area. In addition, a downflow is seen in the line-forming region of the Fe II line. The shocks produced in 3D numerical models (Wedemeyer et al. 2004) produce strong and intermittent temperature fluctuations and are therefore certainly capable of reproducing these conditions, by chance and at random. In this case, Fe II emission events would just be a chance by-product of these fluctuations.

The analysis presented in the previous section provides evidence that the emission events are most probably not purely random processes. Their temporal behavior is quite similar, they are associated with (photospheric) downflows, they are always accompanied by a significant enhancement of the inner wings of the Ca II H line (*calcium mustaches*) and they are systematically linked to H2v brightenings and Doppler shifts of the Ca II H line core. However, 99.99% of the time, the atmosphere is in the chaotic state described by the simulations. This leads to the concluding question: is there a process that is able to dominate over the ubiquitous shocks locally and for a short time to produce the observed Fe II emissions, or are the conditions for Fe II emissions in principle always fulfilled, but are destroyed (or hidden) most of the time by the waves and shocks that are present in the solar atmosphere?

Acknowledgements. The 2007 and 2008 observing campaigns were conducted together with R. Hammer and W. Rammacher. R. Hammer and R. Rezaei provided important and useful comments on the manuscript. The referee report helped to improve the paper. The VTT is operated by the KIS at the Observatorio del Teide of the Instituto de Astrofísica de Canarias in Tenerife, Spain.

References

- Avrett, E. H., & Loeser, R. 2008, *ApJS*, 175, 229
 Balthasar, H. 1984, *Sol. Phys.*, 93, 219
 Beck, C., Rezaei, R., & Puschmann, K. G. 2013a, *A&A*, 556, A127
 Beck, C., Rezaei, R., & Puschmann, K. G. 2013b, *A&A*, 553, A73
 Berkefeld, T., Soltau, D., & von der Lühe, O. 2003, in *Proc. SPIE 4839*, eds. P. L. Wizinowich, & D. Bonaccini, 544
 Borrero, J. M., Martínez-Pillet, V., Schlichenmaier, R., et al. 2010, *ApJ*, 723, L144
 Carlsson, M., & Stein, R. F. 1997, *ApJ*, 481, 500
 Cram, L. E., Lites, B. W., & Rutten, R. J. 1980, *ApJ*, 241, 374
 Doerr, H.-P., Steinmetz, T., Holzwarth, R., Kentischer, T., & Schmidt, W. 2012, *Sol. Phys.*, 59
 Engvold, O., & Halvorsen, H. D. 1973, *Sol. Phys.*, 28, 23
 Evershed, J. 1929, *MNRAS*, 89, 566
 Kneer, F. 2010, *Mem. Soc. Astron. It.*, 81, 604
 Lites, B. W. 1974, *A&A*, 33, 363
 Moore, C. E., Minnaert, M. G. J., & Houtgast, J. 1966, *The solar spectrum 2935 Å to 8770 Å* (Washington: US Government Printing Office)
 Rammacher, W., Schmidt, W., & Hammer, R. 2007, *Astron. Nachr.*, 328, 657
 Rezaei, R., Bruls, J. H. M. J., Schmidt, W., et al. 2008, *A&A*, 484, 503
 Rutten, R. J. 2012, *Roy. Soc. London Philos. Trans. Ser. A*, 370, 3129
 Rutten, R. J., & Stencel, R. E. 1980, *A&AS*, 39, 415
 Schmidt, W., Muglach, K., & Knölker, M. 2000, *ApJ*, 544, 567
 Schmidt, W., Solanki, S. K., Barthol, P., et al. 2010, *Astron. Nachr.*, 331, 601
 Severny, A. B. 1956, *The Observatory*, 76, 241
 Solanki, S. K., Barthol, P., Danilovic, S., et al. 2010, *ApJ*, 723, L127
 Stencel, R. E. 1973, *Sol. Phys.*, 33, 59
 Stencel, R. E. 1977, *ApJ*, 215, 176
 Švestka, Z. 1972, *ARA&A*, 10, 1
 Tritschler, A., Schmidt, W., Uitenbroek, H., & Wedemeyer-Böhm, S. 2007, *A&A*, 462, 303
 Vernazza, J. E., Avrett, E. H., & Loeser, R. 1981, *ApJS*, 45, 635
 von Uexkuell, M., & Kneer, F. 1995, *A&A*, 294, 252
 Wallace, L., Hinkle, K., & Livingston, W. 1998, *An atlas of the spectrum of the solar photosphere from 13 500 to 28 000 cm⁻¹ (3570 to 7405 Å)* (ESO)
 Watanabe, T., & Steenbock, W. 1986, *A&A*, 165, 163
 Wedemeyer, S., Freytag, B., Steffen, M., Ludwig, H.-G., & Holweger, H. 2004, *A&A*, 414, 1121
 Wedemeyer-Böhm, S., Lagg, A., & Nordlund, Å. 2009, *Space Sci. Rev.*, 144, 317
 Wöger, F., Wedemeyer-Böhm, S., Schmidt, W., & von der Lühe, O. 2006, *A&A*, 459, L9